nature photonics

LETTERS

PUBLISHED ONLINE: 22 FEBRUARY 2016 | DOI: 10.1038/NPHOTON.2016.11

Highly efficient quantum dot near-infrared light-emitting diodes

Xiwen Gong‡, Zhenyu Yang‡, Grant Walters, Riccardo Comin, Zhijun Ning†, Eric Beauregard, Valerio Adinolfi, Oleksandr Voznyy and Edward H. Sargent*

Colloidal quantum dots (CQDs) are emerging as promising materials for constructing infrared sources in view of their tunable luminescence, high quantum efficiency and compatibility with solution processing[1]. However, CQD films available today suffer from a compromise between luminescence efficiency and charge transport, and this leads to unacceptably high power consumption. Here, we overcome this issue by embedding CQDs in a high-mobility hybrid perovskite matrix. The new composite enhances radiative recombination in the dots by preventing transport-assisted trapping losses; yet does so without increasing the turn-on voltage. Through compositional engineering of the mixed halide matrix, we achieve a record electroluminescence power conversion efficiency of 4.9%. This surpasses the performance of previously reported CQD near-infrared devices two-fold, indicating great potential for this hybrid QD-in-perovskite approach.

Near-infrared (NIR) light-emitting diodes (LEDs) are used in a wide range of applications including night vision[2], biomedical imaging[3], optical communications and computing[4]. Whereas advanced materials such as organic dyes and semiconductor polymers have shown great benefits in visible lighting[5,6], they have so far failed to produce efficient NIR LEDs because of their large bandgap; to the extent that their band edge can be redshifted, this consistently results in a low photoluminescence quantum yield in the NIR regime[7]. In light of the high luminescence efficiency, emission wavelength tunability, and solution processability of CQDs, researchers have invested considerable efforts in exploring NIR-emitting devices based on these materials[1], and reported power conversion efficiencies (PCE) have recently reached 2.4%[8].

The PCE is defined as the ratio of the output optical power (P_{out}) to the input electrical power (P_{in}). Combined with the definition of external quantum efficiency (EQE)[6], the PCE can be written:

$$\mathrm{PCE} = \frac{P_{out}}{P_{in}} = \frac{P_{out}}{IV} = \frac{\mathrm{EQE}h\nu}{eV} = \frac{\eta_{tot}\eta_{out}h\nu}{eV} \quad (1)$$

$$\eta_{tot} = \frac{n_{charges}}{n_{photons}} = \eta_{diff}\eta_{inj}\chi\eta_{PLQE} \quad (2)$$

where η_{tot} is the fraction of injected charges ($n_{charges}$) that produce the emission of photons from the CQDs; η_{out} is the fraction of emitted photons ($n_{photons}$) that are coupled out of the device; $h\nu$ is the energy of the emitted photons; e is the elementary charge; and V is the voltage applied to the device. η_{diff} is the fraction of injected carriers that successfully diffuse to a QD; η_{inj} is the fraction of these carriers that transfer into a QD and form excitons; χ is the fraction of these excitons whose states have spin-allowed optical transitions (for CQDs, $\chi = 1$) and η_{PLQE} is the internal CQDs photoluminescence quantum efficiency (PLQE) associated with radiative emission from a CQD-localized exciton.

It is clear that high η_{tot} and low V are key parameters for high PCE. Unfortunately, luminescence efficiencies of CQD films, especially for NIR CQDs[9], are generally very low. This is the result of self-quenching, wherein inter-dot transport facilitates transport-assisted trapping, leading to recombination even at relatively rare defect sites[10]. Materials with highly mobile carriers, such as close-packed CQD films, can also exhibit exciton dissociation, and this competes with the radiative recombination and further enhances self-quenching[11].

Strategies to prevent self-quenching in CQD films typically include the growth of a protective shell[12], capping with insulating organic ligands[9] and incorporation into a polymer matrix[9,13,14]. However, these solutions lead to increased power consumption as a higher voltage is required to inject sufficient current to achieve bright light emission. This trade-off between non-radiative recombination and charge transport has persisted, and accounts for the modest PCEs of CQD-based LEDs.

We took the view that QDs combined with perovskite[15,16] could potentially overcome the trade-off between quantum efficiency and voltage efficiency: the perovskite matrix would provide a long diffusion length to enhance η_{diff}, even when CQDs epitaxially embedded in the matrix were widely spaced with the goal of avoiding self-quenching and exciton dissociation (Fig. 1a). The epitaxial interface[15] between the perovskite matrix and the CQDs would serve to provide excellent passivation, improving both η_{inj} and η_{PLQE}. The use of a type-I band alignment would enable electrons and holes to be funnelled efficiently from the matrix and be confined in the CQDs, again preventing exciton dissociation losses.

Previous works on QD:perovskite solids suffered from a lattice mismatch (~5%) between iodide-based perovskite and PbS nanocrystals. We explored variations in the perovskite lattice constant via mixing of iodide and bromide (Fig. 1a,b). The PLQE of QD inclusions and the carrier transport in the matrix are greatly increased in the mixed-halide perovskite matrix ($MAPbI_xBr_{3-x}$) compared with the first generation quantum-dot-in-perovskites that relied on $MAPbI_3$ (ref. 15). The introduction of bromide also enables a pinhole-free morphology and improves the carrier diffusion length in the perovskite matrix, resulting in lower trap-assisted recombination and consequently in more efficient emission from the active layer.

Our LED device architecture is described in Fig. 1b: indium tin oxide (ITO)/titanium dioxide (TiO_2, 10 nm)/dots-in-perovskite emission layer (350 nm) (Fig. 1c)/poly(9,9′-dioctylfluorene)

Department of Electrical and Computer Engineering, University of Toronto, 10 King's College Road, Toronto, Ontario M5S 3G4, Canada. †Present address: School of Physical Science and Technology, ShanghaiTech University, Haike Road 100, 201210 Shanghai, China. ‡These authors contributed equally to this work. *e-mail: ted.sargent@utoronto.ca

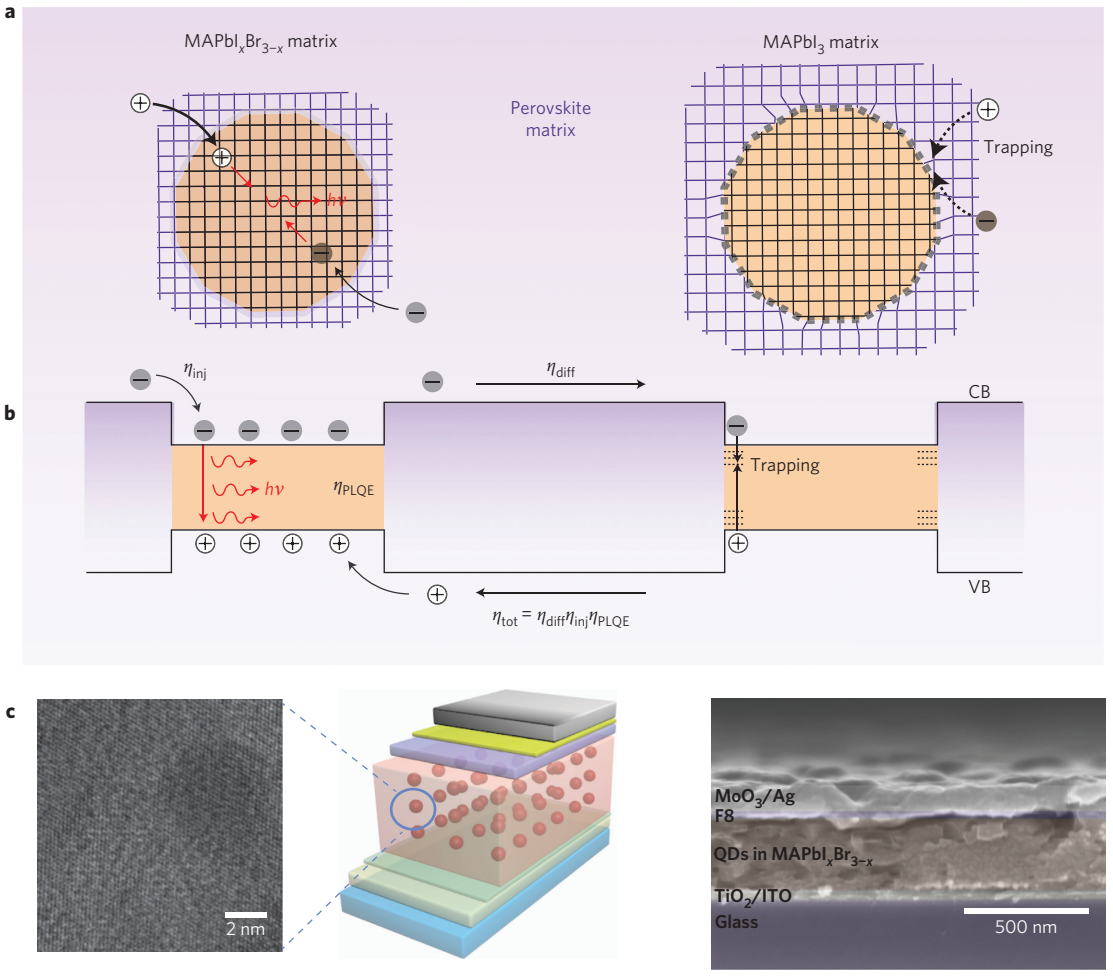

Figure 1 | QD-in-perovskite LED device architecture. a, Illustration of enhanced electroluminescence efficiency in PbS QDs in $MAPbX_3$ (X = I, Br) perovskite CQD LEDs, the left panel illustrates that radiative recombination dominates when QDs and perovskite are lattice matched, whereas lattice mismatch causes interfacial defects (black dash line) and non-radiative recombination through traps (right panel). **b**, The corresponding spatial band diagram shows the mechanism of carrier transport, injection and recombination, illustrating the key parameters that are essential for highly efficient QD LEDs. **c**, HRTEM images of a PbS QD in a perovskite matrix (left), the LED device architecture used in this study (middle) and the corresponding cross-section SEM image of same device (right).

(F8, 50 nm)/molybdenum trioxide (MoO_3, 6 nm)/silver (Ag, 100 nm). As seen from the calculated band diagram for the LED device at zero bias (Supplementary Fig. 1, top panel), the energy levels of the F8 and TiO_2 layers are suitably aligned with the perovskite matrix to serve as electron- and hole-blocking layers, respectively, while enabling selective injection of the desired carrier type into the active layer. In addition, a type-I heterojunction between the QD acceptor levels (dashed black line) and perovskite band edges (blue and red line for the conduction and valence band, respectively) is maintained throughout the emissive QD-in-perovskite layer. Under forward bias (Supplementary Fig. 1, bottom panel) electrons and holes are injected from the cathode (TiO_2) and anode (F8), respectively, and they are efficiently transferred to the QDs, where they recombine radiatively.

The EQE curves (Fig. 2a) highlight the efficiency increase on incorporation of small amounts of bromine, with a maximum EQE value of 3.8% for a matrix with 83% iodine molar concentration (the molar ratio between iodine and all halides). The EQE is 2.3× higher than for the pure $MAPbI_3$ matrix. However, EQE drops with lower iodine content, with no NIR light emission for iodide molar concentrations below 67%. To investigate the origins of the matrix composition-dependent electroluminescence of CQDs, we further investigated the photophysical properties of QDs in the $MAPbI_xBr_{3-x}$ matrix.

The first important function of the perovskite matrix is to transport photogenerated carriers into the QDs. We found that the diffusion length (Fig. 2b), which will determine the efficiency with which electron–hole pairs can be delivered to the CQDs, shows a significant enhancement once bromine is incorporated into the matrix[17]. The diffusion length and the photoluminescence lifetime (Supplementary Fig. 2) both peak at 83% iodine halide content. This perovskite matrix also shows the best stability in moist air (Supplementary Fig. 3).

We then studied the quality of the interface between QDs and perovskite. Figure 2c shows that the PLQE of CQDs photoexcited below the perovskite bandgap increases with higher bromine concentration and peaks at 50% iodine concentration. As in previous work[15], the perovskite matrix epitaxially grows around the QDs, providing a natural passivation of the CQD surface, and this leads to higher η_{PLQE} and η_{inj}. We propose that the further improved lattice matching reported herein through the use of the mixed halide matrix reduces strain at the heteroepitaxial interface, and further lowers the density of defects. We measured powder X-ray diffraction of pure QDs and in the $MAPbI_xBr_{3-x}$ perovskite matrix to evaluate the lattice mismatch (Supplementary Fig. 4). As the PbS lattice constant (5.91 Å) lies between that of $MAPbI_3$ (6.26 Å) and $MAPbBr_3$ (5.89 Å), the lattice matching improves with increasing bromine concentration and peaks at 67% iodine content, where the interface exhibits the lowest strain.

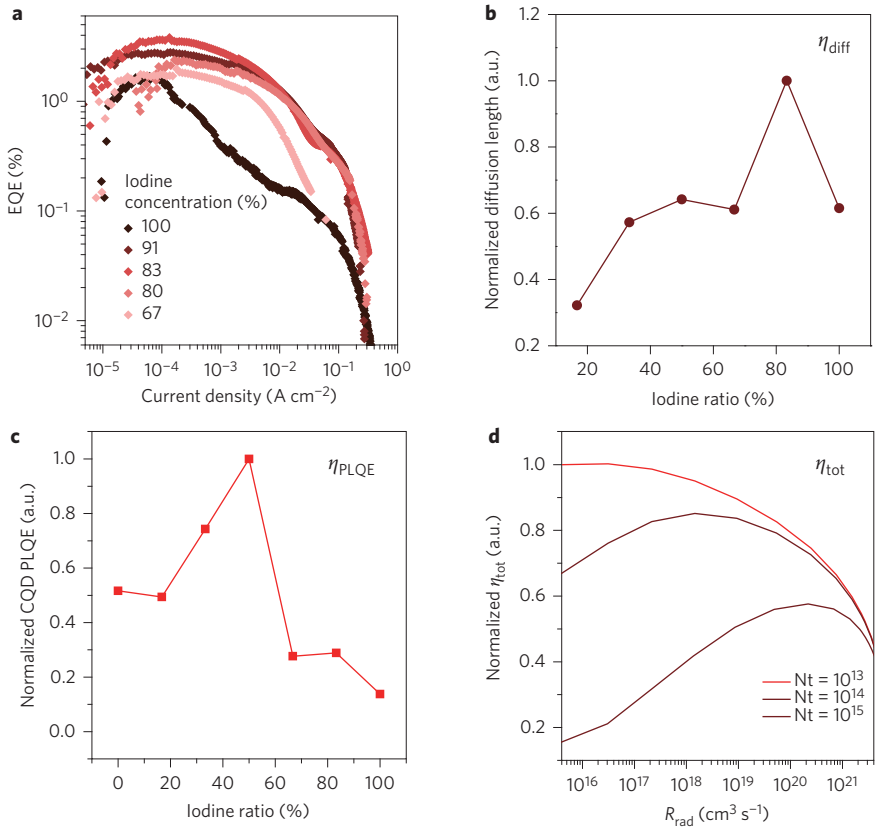

Figure 2 | Device performance and photoluminescent properties of CQDs in $MAPbI_xBr_{3-x}$ perovskite. a, EQE–current density performance of CQDs in mixed halide perovskite LEDs with various iodine molar concentrations. **b**, Normalized diffusion length of the mixed halide perovskite. **c**, PLQE of PbS QDs in $MAPbI_xBr_{3-x}$. **d**, η_{tot} at different radiative recombination rates (R_{rad}) with different defect densities (Nt) of the active layer.

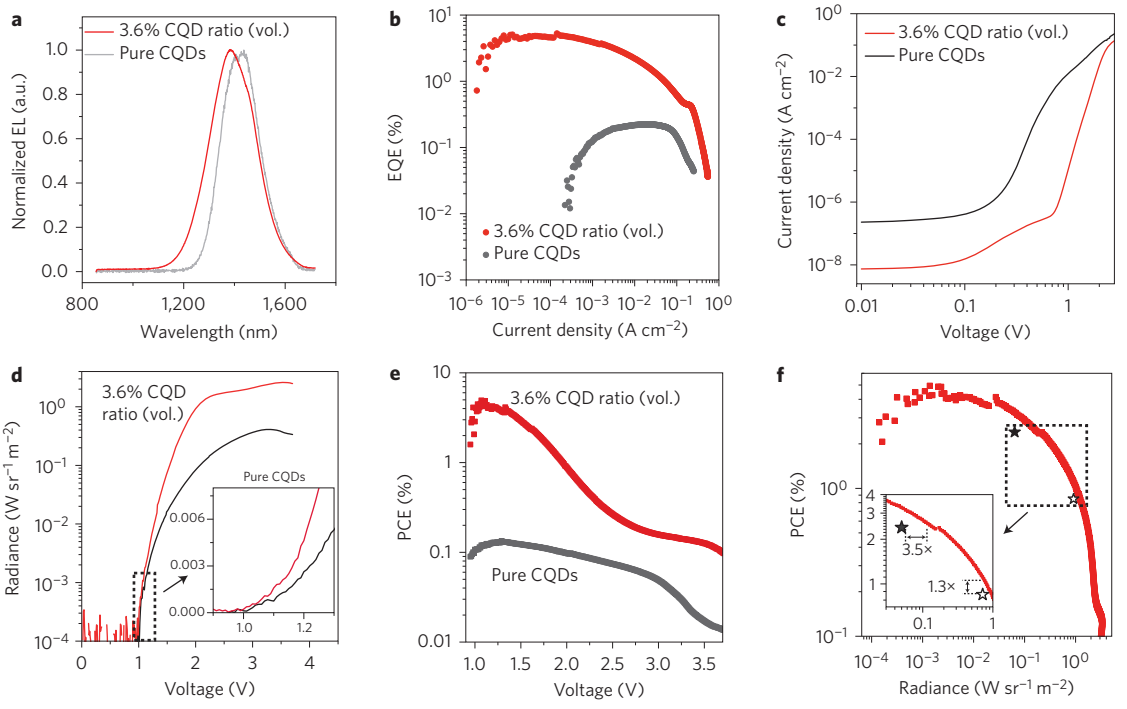

Figure 3 | EL performance of QD-in-perovskite LEDs emitting at 1,391 nm. a, EL spectra (applied voltage, 2 V). **b**, EQE–current density performance. **c**, Current density–voltage curves. **d**, Radiance–voltage characteristics. Inset: Zoom-in region of radiance–voltage plots (0.9–1.3 V) showing device turn-on voltages. **e**, PCE–voltage performance for champion CQD-in-perovskite devices (3.6% volume ratio) matrix versus a pure CQD device. **f**, PCE–radiance performance of champion device compared with the current published record[8] (solid star, radiance under PCE maximum; empty star, PCE under radiance maximum in the reference). Inset: Zoom-in region of radiance–PCE plot.

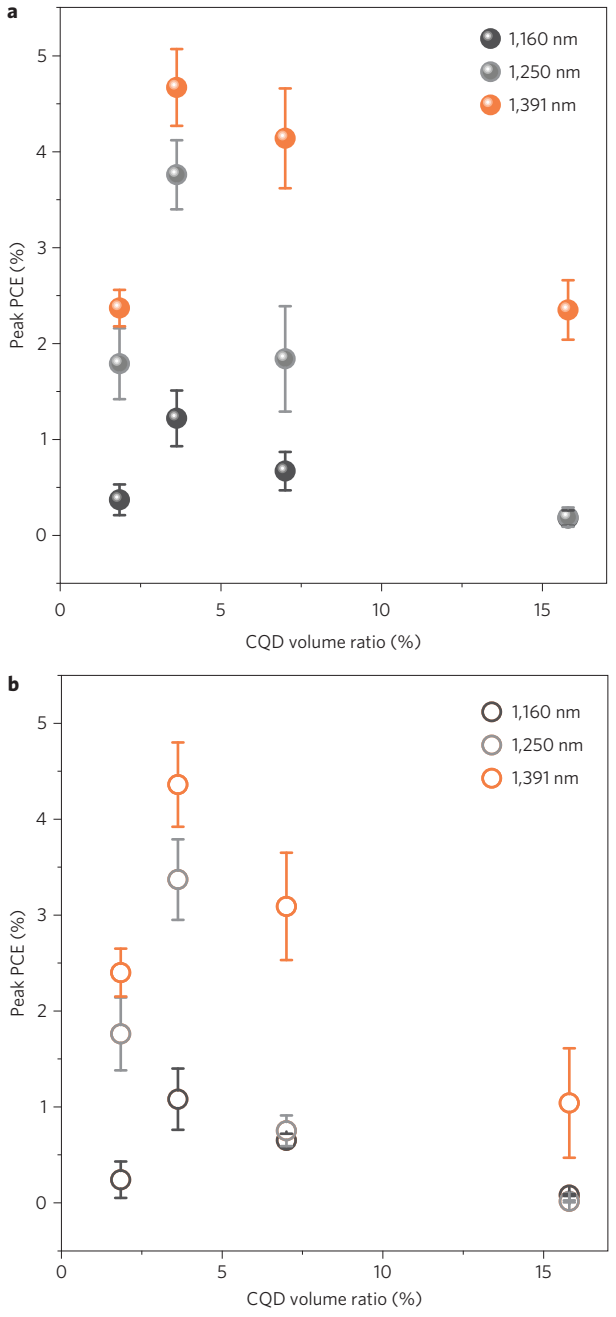

Figure 4 | Size tunability of CQDs in NIR LEDs. a,**b**, Average peak EQE (**a**) and PCE (**b**) values of QD-in-perovskite devices with various CQD:perovskite volume ratios and device emission wavelengths. Error bars represent the standard deviation of several devices.

In sum, the addition of bromine reduces the defect density both inside the perovskite matrix and on the CQD surface, improving diffusion efficiency and PLQE. Reduced non-radiative recombination losses should result in higher total luminescence efficiency of the material. Our optoelectronic device modelling shows that trap recombination is the most detrimental mechanism at low driving voltages (low brightness regime) whereas at higher injection densities Auger recombination becomes the dominant loss. Simulations in Fig. 2d show that across the entire range of achievable LED brightnesses, devices with the lowest trap densities give the highest η_{tot}, highlighting the importance of controlling trap-related losses in the conductive active layer.

When CQDs are evenly distributed in the perovskite matrix at low concentrations, the electroluminescence (EL) properties are dramatically improved compared with pure CQD-based devices. The strongest EL intensity observed in this work was from devices emitting at 1,391 nm. The blueshift in the EL signal from CQD-in-perovskite devices compared with CQD-only counterparts is consistent with the shift in PL (Fig. 3a and Supplementary Fig. 5). We attribute the EL enhancement to the reduced self-quenching and excellent passivation from perovskite, especially for low CQD concentrations at which dots are well separated from one other (Fig. 4a). The best EQE is attained at 3.6% CQDs. The best devices emit at 1,391 nm with an EQE of 5.2 ± 0.3% (Fig. 3b). The average value for all measured devices is 4.7 ± 0.4% (Fig. 3f), comparable to the average for previously reported core–shell PbS/CdS CQD-based LEDs[8]. The EQE value is 150× higher than that of a CQD-only control device (EQE = 0.03 ± 0.01%).

Compared with other matrix materials such as polymers and inorganic crystals, the best perovskites exhibit considerably lower trap densities and higher mobility[18]. This will beneficially affect the driving voltage required to achieve high brightness and thus the power conversion efficiency (Supplementary Fig. 6c), a figure of particular relevance to practical device operation. To study how EQE translates into PCE, we investigated the current–voltage (J–V) characteristics in greater detail (Fig. 3c). The higher current density observed in the pure CQD device is due to the smaller bandgap (0.89 eV for the CQD versus 1.73 eV for the device with a perovskite matrix) and a reduced thickness of the active layer. In the QD-in-perovskite devices, the current density is considerably lower at low applied voltages, producing a higher EQE. We attribute this, once again, to the epitaxially aligned CQD/perovskite interface that passivates CQD trap states and reduces non-radiative recombination.

We determined a turn-on voltage of 1.0 V for the matrix-based LEDs (Fig. 3d), indicating effective carrier injection from the charge transport layer to the CQD inclusions. The brightness at each voltage is dramatically improved. For example, we measured a peak radiance of 2.6 Wsr^{-1} m^{-2} at 3.5 V applied voltage, which is ~15× higher than the control pure CQD device (Supplementary Fig. 7). A similar increase in radiance is also found in matrix-based devices with smaller embedded dots emitting at 1,250 nm (Supplementary Fig. 8).

The combination of relatively high radiance and absolute output power, together with high EQE with low driving voltage, allows notable improvements in PCE values relative to previous reports (Fig. 3e). A peak PCE of 4.9% is obtained at 1.1 V; more than 2× higher than previous record values for IR CQD EL (Supplementary Table 1)[8]. The PCE values exceed 1% in the full range 1–2 V, beyond which they maintain high radiance (up to 0.92 W sr^{-1} m^{-2}).

In sum, the perovskite-matrix-based devices simultaneously achieve both high radiance and efficiency (Fig. 3f). The device radiance at maximum PCE is ~3.5× higher than in previous record CQD IR EL devices[8]; similarly, the PCE at maximum radiance is also improved.

We demonstrated the same architecture and physical principles using a number of different CQDs sizes. Consistent with the PLQE results (Supplementary Fig. 9), both the peak EQE and PCE average values increase as the CQD size increases (Fig. 4). Although there is some variance at lower CQD concentrations, the EQE and PCE values are both maximized in devices with low CQDs loadings (3.6% volume ratio). In particular, the EQE values decrease significantly at higher CQD concentrations (for example, 16% volume ratio), a behaviour we ascribe to the imperfect passivation by the perovskite matrix and the formation of dot-to-dot intercommunication channels. However, regardless of the perovskite/CQD ratio and emission wavelength, all CQD-in-perovskite LEDs exhibited higher EQE and PCE values than those based on pure CQDs as emissive layers, suggesting that the type-I architecture is still beneficial even at high CQD loadings.

In conclusion, we have developed an original platform for bright NIR-LEDs. The work builds on a recent report of QD-in-perovskite materials and significantly augments these recent findings by creating an efficient EL-compatible matrix. Thanks to the excellent diffusion length of the iodide/bromide mixed perovskite, as well as its type-I band alignment, charge carriers are transported through the perovskite matrix to efficiently recombine in CQDs. This yields devices with a tunable emission wavelength, band edge-derived turn-on voltages, and record power efficiencies. The results highlight the potential of these emerging materials for power-efficient, low-cost and large-area LEDs and displays.

Methods

Methods and any associated references are available in the online version of the paper.

Received 17 April 2015; accepted 15 January 2016; published online 22 February 2016

References

1. Bourdakos, K. N., Dissanayake, D. M. N. M., Lutz, T., Silva, S. R. P. & Curry, R. J. Highly efficient near-infrared hybrid organic-inorganic nanocrystal electroluminescence device. *Appl. Phys. Lett.* **92,** 90–93 (2008).
2. Sun, L. *et al.* Bright infrared quantum-dot light-emitting diodes through inter-dot spacing control. *Nature Nanotech.* **7,** 369–373 (2012).
3. Medintz, I. L., Uyeda, H. T., Goldman, E. R. & Mattoussi, H. Quantum dot bioconjugates for imaging, labelling and sensing. *Nature Mater.* **4,** 435–446 (2005).
4. Sargent, E. H. Infrared quantum dots. *Adv. Mater.* **17,** 515–522 (2005).
5. Kim, K.-H. *et al.* Phosphorescent dye-based supramolecules for high-efficiency organic light-emitting diodes. *Nature Commun.* **5,** 4769 (2014).
6. Sekine, C., Tsubata, Y., Yamada, T., Kitano, M. & Doi, S. Recent progress of high performance polymer OLED and OPV materials for organic printed electronics. *Sci. Technol. Adv. Mater.* **15,** 034203 (2014).
7. Shirasaki, Y., Supran, G. J., Bawendi, M. G. & Bulović, V. Emergence of colloidal quantum-dot light-emitting technologies. *Nature Photon.* **7,** 13–23 (2013).
8. Supran, G. J. *et al.* High-performance shortwave-infrared light-emitting devices using core–shell (PbS–CdS) colloidal quantum dots. *Adv. Mater.* **27,** 1437–1442 (2015).
9. Tessler, N., Medvedev, V., Kazes, M., Kan, S. & Banin, U. Efficient near-infrared polymer nanocrystal light-emitting diodes. *Science* **295,** 1506–1508 (2002).
10. Zhitomirsky, D., Voznyy, O., Hoogland, S. & Sargent, E. H. Measuring charge carrier diffusion in coupled colloidal quantum dot solids. *ACS Nano* **7,** 5282–5290 (2013).
11. Choi, J. J. *et al.* Photogenerated exciton dissociation in highly coupled lead salt nanocrystal assemblies. *Nano Lett.* **10,** 1805–1811 (2010).
12. Moroz, P. *et al.* Infrared emitting PbS nanocrystal solids through matrix encapsulation. *Chem. Mater.* **26,** 4256–4264 (2014).
13. Greenham, N., Peng, X. & Alivisatos, A. Charge separation and transport in conjugated-polymer/semiconductor-nanocrystal composites studied by photoluminescence quenching and photoconductivity. *Phys. Rev. B* **54,** 17628–17637 (1996).
14. Steckel, J. S., Coe-Sullivan, S., Bulović, V. & Bawendi, M. G. 1.3 μm to 1.55 μm tunable electroluminescence from PbSe quantum dots embedded within an organic device. *Adv. Mater.* **15,** 1862–1866 (2003).
15. Ning, Z. *et al.* Quantum-dot-in-perovskite solids. *Nature* **523,** 324–328 (2015).
16. Hu, L. *et al.* PbS colloidal quantum dots as an effective hole transporter for planar heterojunction perovskite solar cells. *J. Mater. Chem. A* **3,** 515–518 (2015).
17. Jeon, N. J. *et al.* Compositional engineering of perovskite materials for high-performance solar cells. *Nature* **517,** 476–480 (2015).
18. Shi, D. *et al.* Low trap-state density and long carrier diffusion in organolead trihalide perovskite single crystals. *Science* **347,** 519–522 (2015).

Acknowledgements

This publication is based in part on work supported by an award (KUS-11-009-21) from the King Abdullah University of Science and Technology (KAUST), by the Ontario Research Fund Research Excellence Program, and by the Natural Sciences and Engineering Research Council (NSERC) of Canada. X.G. thanks Mitacs for a Globalink Graduate Fellowship Award. The authors thank L. Levina for assistance in CQD synthesis; X. Lan, E. Yassitepe and F. Fan for acquiring microscopic images; and E. Palmiano, R. Wolowiec, and D. Kopilovic for their help during the course of study.

Author contributions

X.G., Z.Y., Z.N., and E.H.S. designed and directed this study. X.G. and Z.Y. contributed to all the experimental work. G.W. and E.B. carried out the PLQE measurements and analysis. R.C. performed PL decay measurement and analysis. V.A., O.V. and X.G. performed optoelectronic simulation. X.G., Z.Y., R.C., and E.H.S. wrote the manuscript.

Additional information

Supplementary information is available in the online version of the paper. Reprints and permissions information is available online at www.nature.com/reprints. Correspondence and requests for materials should be addressed to E.H.S.

Competing financial interests

The authors declare no competing financial interests.

Methods

CQD synthesis and solution exchange. CQDs are synthesized using methods previously reported[19]. For the iodide ligand exchange, 3 ml of CQDs dispersed in octane (10 mg ml^{-1}) are added to a 3 ml dimethylformamide (DMF) solution containing 695 mg of PbI_2 and 240 mg of CH_3NH_3I. After the CQDs are stirred vigorously for 15 min, they transfer from the top octane phase to the bottom DMF layer.

The octane layer is then decanted and the CQD solution is washed three more times with octane to remove any organic residue. Subsequently, the CQDs are precipitated by the addition of toluene. The sample is centrifuged and the solution decanted. The CQDs are dried for 10 min under vacuum and weighed. The nanoparticles are dispersed in butylamine for film fabrication.

QD-in-perovskite solids fabrication. The desired amount of the perovskite precursor (PbI_2 and $PbBr_2$ with one quarter weight ratio of CH_3NH_3I) in butylamine is added to the exchanged CQDs. The solution is spin-coated (6,000 rpm, 10 s) onto the substrate, and then annealed at 70 °C for 10 min in an N_2 glovebox to remove butylamine completely from the film[15]. For perovskite growth, a methylammonium halide mixed solution (10 mg ml^{-1} in isopropanol) is drop-cast on the film and removed after 30 s by spin coating (6,000 rpm, 10 s), after which the film is soaked in pure isopropanol for 10 s, and the substrate is again spun (6,000 rpm, 10 s) for complete removal of the residual solvent. The QD-in-perovskite film is annealed again at 70 °C for 10 min in an N_2 glovebox.

Fabrication of LEDs. Pre-patterned ITO-coated glass substrates are treated using an oxygen plasma for 10 min immediately before use. The TiO_2 layer is fabricated by a two-step method: the initial layer is deposited at 150 °C using atomic layer deposition (ALD) (Cambridge Savannah S100 ALD system) using tetrakis (dimethylamido) titanium (IV) and water as precursors, and the film is then further treated by $TiCl_4$ aqueous solutions (40 mM) at 70 °C for 30 min. This is followed by washing with deionized water, drying by N_2 flow, and finally, annealing at 400 °C for 1 h. Once cool, the substrates are stored in an N_2 glovebox for further use. The F8/chlorobenzene solution (10 mg ml^{-1}) is annealed at 90 °C under a nitrogen atmosphere and spin-cast onto the QD-in-perovskite layer at 70 °C and 3,000 rpm for 60 s to form a uniform hole transport layer. The top electrode, consisting of 6 nm of MoO_3 and 100 nm of Ag, is deposited by thermal evaporation at a pressure $<1 \times 10^{-6}$ Torr. Each ITO substrate (2.5 cm × 2.5 cm) is patterned to yield eight devices, each with an area of 3.1 mm^2.

PL and EL measurement. PL measurements are performed using a Horiba Fluorolog time-correlated single-photon counting system with photomultiplier tube detectors. A monochromatized Xe lamp and pulsed laser diodes were used as excitation sources for steady-state and transient measurements, respectively. Absolute PLQE measurements were carried out in a Quanta-Phi integrating sphere according to standard methods published elsewhere[20]. The diffusion length of perovskite matrix was obtained by measuring the PL decay with a reported quenching method, and subsequently fitting the dynamics with a 1D diffusion equation[21]. For EL measurement, devices are characterized using a Keithley 2,410 source meter. Under a range of forward bias voltages, the EL spectra are collected through a set of lenses focused on an optical fiber and connected to the NIR spectrophotometer (Ocean Optics, NIR-512).

Device performance characterization. The radiated power of EL was measured using a calibrated Ophir PD300-IR germanium photodiode (active area: 19.6 mm^2) and recorded *in situ* using a computer-controlled Keithley 2,400 source meter under a nitrogen atmosphere and in parallel with the *J*–*V* measurements. Lambertian emission was assumed in the calculation of EQE and radiance. Peak EQE was determined as the number of forward-emitted photons to the number of injected electrons. A geometric correction factor was used according to the distance between the photodiode and device and the active area of the detector. PCE was calculated as the radiative EL power divided by the total input electrical power. For each type of sample (for example, specific QD versus perovskite concentration and the size of the quantum dot), at least five devices were tested for each EQE and PCE calculations.

Optoelectronic simulation. Device simulations were performed in SCAPS 3. 0.01 software[22]. Ohmic boundary conditions were assumed on each side. Material parameters were based on data previously used in CQD solar cell simulations[23]. Trap densities of 10^{13}, 10^{14} and 10^{15} cm^{-3} were chosen.

References

19. Hines, M. A. & Scholes, G. D. Colloidal PbS nanocrystals with size-tunable near-infrared emission: observation of post-synthesis self-narrowing of the particle size distribution. *Adv. Mater.* **15,** 1844–1849 (2003).
20. De Mello, J. C., Wittmannn, H. F. & Friend, R. H. An improved experimental determination of external photoluminescence quantum efficiency. *Adv. Mater.* **9,** 230 (1997).
21. Xing, G. *et al.* Long-range balanced electron- and hole-transport lengths in organic-inorganic $CH_3NH_3PbI_3$. *Science* **342,** 344–347 (2013).
22. Burgelman, M., Nollet, P. & Degrave, S. Modelling polycrystalline semiconductor solar cells. *Thin Solid Films* **527,** 361–362 (2000).
23. Zhitomirsky, D. *et al.* Engineering colloidal quantum dot solids within and beyond the mobility-invariant regime. *Nature Commun.* **5,** 3803 (2014).